$CeIr_3$: Superconductivity in a phase based on Tetragonally Close Packed (TCP) clusters

Karolina Górnicka[1], Elizabeth M. Carnicom[2], Sylwia Gołąb[3], Marcin Łapiński[1], Bartłomiej Wiendlocha[3], Weiwei Xie[4], Dariusz Kaczorowski[5], Robert J. Cava[2] and Tomasz Klimczuk[1]

[1] *Faculty of Applied Physics and Mathematics, Gdansk University of Technology, ul. Narutowicza 11/12, 80-233 Gdańsk, Poland, e-mail: karolina.gornicka@pg.edu.pl*

[2] *Department of Chemistry, Princeton University, Princeton, NJ 08544, USA*

[3] *Faculty of Physics and Applied Computer Science, AGH University of Science and Technology, Aleja Mickiewicza 30, 30-059 Kraków, Poland*

[4] *Department of Chemistry, Louisiana State University, Baton Rouge LA 70803*

[5] *Institute of Low Temperature and Structure Research, Polish Academy of Sciences, P. O. Box 1410, 50-950 Wrocław, Poland*

Abstract

We present the crystallographic analysis, superconducting and spectroscopic characterization, and theoretical modeling of $CeIr_3$. Lattice parameters a = 5.2945(1) Å and c = 26.219(1) Å are found for the *R-3m* symmetry crystal structure, which are close to the literature values. $CeIr_3$ is a moderate type-II superconductor (κ_{GL} =17, $\lambda_{e\text{-}p}$ = 0.65) below 2.5 K. Ce ions exhibit strongly intermediate valence character as evidenced by X-ray photoelectron spectroscopy. The normal state magnetic susceptibility is weakly temperature dependent and follows the inter-configuration fluctuation model with a singlet Ce - $4f^0$ ground state. Theoretical calculations support a non-magnetic ground state of the system and reveal that Ir - 5*d* states are dominant at the Fermi level.

Introduction

For several years, superconductivity emerging on the verge of electronic instability, e.g. of magnetic nature, has attracted much attention owing to its possible unconventional character. In this context, materials bearing *d*- and *f*- electrons are particularly interesting, since their electronic properties are often dominated by strong spin-orbit coupling. Recently, within the family of Ce-based heavy fermion superconductors (HFS),[1,2] the most intensively studied compounds have been those from a homologous series $Ce_nT_mIn_{3n+2m}$, where T = Co, Rh, Ir, Pd or Pt, forming with tetragonal crystal structures built of n layers of $CeIn_3$ ($AuCu_3$ type) and m layers of TIn_2 ($HgTe_2$ type).

A related homologues series[3] is $RE_{2m+n}T_{4m+5n}$, where m and n represent the number of $MgCu_2$- and $CaCu_5$-type blocks, respectively. In this formula, *RE* stands for an early rare earth metal (La – Gd) and *T* is a transition metal: Ir or Rh. In contrast to $Ce_nT_mIn_{3n+2m}$, this series has not been intensively studied and only a few compounds with the stoichiometry RET_3 (m = 1, n = 1) and RE_2T_7 (m = 1, n = 2) have been reported[4,5]. This is likely caused by a difficult synthesis process. Although a binary compound in this group, $CeIr_3$, was reported as a superconductor more than 50 years ago[5] anddetails on its superconducting state were reported only recently[6]. Here, we describe the synthesis and characterization of polycrystalline $CeIr_3$ by means of dc magnetization, electrical resistivity and heat capacity measurements. In addition, in order to examine the valence of Ce ions, an X-ray photoelectron spectroscopy (XPS) study was performed. The experimental data are supplemented by electronic structure calculations.

Experimental

Polycrystalline samples of nominal composition $CeIr_3$, $Ce_{1.03}Ir_3$ and $Ce_{1.05}Ir_3$ were synthesized by arc-melting cerium (4N) and iridium (3N5) in an arc furnace (MAM-1 Edmund Buhler GmbH) on a water-cooled copper hearth using a tungsten electrode under a high purity argon atmosphere. A piece of zirconium was used as an oxygen getter. First, a button of Ir was prepared

by arc-melting iridium powder alone. The Ir ingot was then melted with Ce pieces with 3% excess to compensate for the expected loss of Ce. After the initial melt, the sample button was turned and re-melted 4-5 times to improve homogeneity. Mass loss during the synthesis was lower than 1%, and the sample button formed was uniform, hard and silvery grey in color. The samples obtained were then wrapped in tantalum foil and annealed at 1370˚C for 12 hours under high vacuum (10^{-5} torr). Subsequently, the resulting material was ground well, pressed into a pellet using a hydraulic press and then heated under high vacuum to 1400˚C and held at this temperature for 36 hours.

The crystal structure of $CeIr_3$ was confirmed using a Bruker Apex II X-ray single crystal diffractometer with Mo Kα1 radiation (λ = 0.71073 Å). The room temperature intensity data were collected for a crystal taken from the nominally $Ce_{1.03}Ir_3$ sample, over a full sphere of reciprocal space with 0.5° scans in ω, 10 s per frame of exposure time, and a 2θ ranging from 4° to 75°. The SAINT program[7] was used to both extract intensities and to correct for polarization and Lorentz effects and the XPREP program[8] was used to perform face-indexed numerical absorption corrections. Twinning of the unit cell was tested using the Cell_Now program. The crystal structure of $CeIr_3$ was solved using direct methods and refined by full-matrix least-squares on F^2 with the SHELXTL package[9].

The structure and phase purity of the samples at room temperature was evaluated by powder X-ray diffraction (pXRD) on a Bruker D8 Advance Eco diffractometer (Cu Kα), equipped with a LynxEye-XE detector. X-ray analysis was performed on well-ground powder of the $CeIr_3$ sample. XPS was performed using an Argus (Omicron NanoTechnology) X-ray photoelectron spectrometer. The photoelectrons were excited by a Mg-Kα X-ray source operated at 15 keV and 300 W. The XPS measurement was performed at room temperature under ultra-high vacuum conditions, at pressures below 1.1 $x10^{-8}$ mbar. It is known that cerium on surfaces tends to exist as Ce^{3+} rather than Ce^{4+}.[10] To avoid this potential issue, the $CeIr_3$ sample was sputter-cleaned by Ar ions *in situ* (FDG 150 ion source mounted in the analytic chamber) before the XPS measurement. Data analysis was performed

with the CASA XPS software package using a Shirley background subtraction and least-square Gaussian-Lorentzian curve fitting algorithm. The spectra obtained were calibrated to give a binding energy of 285.00 eV for C 1s.

Magnetization measurements were carried out using a Quantum Design Dynacool Physical Property Measurement System (PPMS) with a vibrating sample magnetometer (VSM) function. Both zero-field-cooled (ZFC) and field-cooled (FC) data were collected from 1.7 – 3 K under an applied field of 20 Oe. The magnetization was also measured at various temperatures in the superconducting state as a function of applied field. ZFC magnetic susceptibility was measured from 3 K to 300 K under 1 kOe field. Resistivity and heat capacity measurements were performed on a PPMS Evercool II. Temperature- and magnetic field-dependent electrical transport measurements were made using a standard four-probe technique. For these experiments, 37-μm-diameter platinum wire leads were spark-welded to the sample surface. The two-τ time- relaxation method was used to measure the specific heat in magnetic fields up to 2 T.

Electronic structure calculations were performed using the full-potential linearized augmented plane-wave method with local orbitals (LAPW+LO) and the Perdew–Burke–Ernzerhof generalized gradient approximation (PBE-GGA) exchange-correlation potential, as implemented in the WIEN2k package[11]. To account for the possible strong Coulomb interaction effect due to the presence of the *4f*-electrons of Cerium, the GGA+U [12] method was used. We determined the magnitude of the U-parameter for the 4*f* states of Ce with the help of the impurity method[13]. As a result, U = 6 eV was obtained, which agrees with the typically used value of the effective U_{eff} = U - J = 5 eV, as J is on the order of 1 eV.[14] This value of the effective U_{eff} = 5 eV was then used in our studies. We also performed additional calculations using the onsite-exact-exchange hybrid Fock approximation[15], with the standard value of the parameter α=0.25 (see, Ref. 15), and both methods gave similar results. The self-interaction correction (SIC) double-counting correction method was used, as the around-mean field (AMF) method predicted quite large magnetic moments on Ce atoms

(0.5 - 1 μ_B), which were not observed in our experiment. The unit cell volume was optimized in the calculations, but the experimental parameters changed only slightly: *a* by about 0.6% and *c* by about 1.1%, which did not significantly affect the calculated electronic structure of this compound. To clarify the effect of Coulomb interactions, both GGA and GGA+U methods were employed, with spin-orbit coupling (SOC) included in each case.

Results and discussion

The single-crystal diffraction experiments confirmed the crystal structure[4] of $CeIr_3$, which forms in the space group *R*-3*m* (No. 166), where *a* = 5.304(4) Å and *c* = 26.273(20) Å. Crystallographic data and the refined positions for a crystal obtained from the nominal $Ce_{1.03}Ir_3$ composition are gathered in **Table 1** and **Table 2**, respectively. It should be noted that the refined stoichiometry of the single crystal studied was $Ce_{0.96(2)}Ir_3$ (from the sample also used for all physical measurements) - within two standard deviations of the ideal 1:3 composition, which is thus taken as the formula of the compound. The space group and lattice parameters obtained were taken as the starting point for the LeBail fit of the powder X-ray diffraction (pXRD) pattern shown in **Figure 1**. The fit is excellent and there is no impurity phase observed in the pXRD pattern of the sample whose properties were studied. The estimated lattice parameters from the LeBail fit (*a* = 5.2945(1) Å, *c* = 26.219(1) Å) are in very good agreement with the single-crystal diffraction results as well as with those reported in the literature[3,4,6,16].

An expanded view of the unit cell and the atomic coordination polyhedra for $CeIr_3$ are shown in **Figure 2**. It has previously been proposed that $CeIr_3$ can be considered as a stacking of cubic $MgCu_2$-type and $CaCu_5$-type layers[3] but the cubic $MgCu_2$-type and rhombohedral $CeIr_3$ structures have different symmetry. Considering the similar polyhedral environments in both cubic and hexagonal Laves phases, we rather describe $CeIr_3$ as a combination of stacking hexagonal $MgZn_2$-type and $CaCu_5$-type layers (**Figure 2**).

The polyhedral environments for all atomic sites in $CeIr_3$ are Frank−Kasper polyhedra[17]. One Ce site is surrounded by a 16-vertex polyhedron consisting of Ir atoms and the other Ce site is centered within a truncated tetrahedron of 12 Ir atoms. The Ir sites are coordinated by distorted icosahedra of 6 Ce and 6 Ir atoms, 3 Ce and 9 Ir atoms, and 5 Ce and 7 Ir atoms. Such Frank−Kasper polyhedra are signature building blocks of tetrahedrally close-packed (tcp) solids. Typical examples of tcp solids include the cubic $MgCu_2$-type and hexagonal $MgZn_2$-type Laves phases, $CaCu_5$-type compounds, and α-Mn. We argue that in this context $CeIr_3$ can best be seen as consisting of stacked layers of $CeIr_2$ in a hexagonal $MgZn_2$-type structure and $CaCu_5$-type $CeIr_5$. These structure types, consisting of densely packed tetrahedral clusters, are known to be good hosts for superconductivity.

For the purposes of the electronic structure calculations, which will be discussed further, a primitive cell must be considered, and so we also present an alternative description of the structure of $CeIr_3$. The primitive cell of $CeIr_3$ contains three formula units. There are two nonequivalent positions of Ce and three of Ir. In the crystal structure shown schematically in the inset of Figure 1 one can distinguish a metallic plane consisting of Ir(18*h*) and a plane consisting of hexagons of Ir(6*c*) centered at Ce(3*a*) - they are Kagome-like 2D sublattices that are also found in the $CeIr_5$ structure. The latter plane is situated in the middle between two metallic planes such that each Ir(6*c*) has six nearest neighbors Ir(18*h*) and form with them two nearly non-distorted tetrahedra (Ir(18*h*)-Ir(18*h*) with a distance equal to 2.64 Å and Ir(18*h*)-Ir(6*c*) - 2.66 Å). Ce(6*c*) has six in-plane nearest neighbors Ir(18*h*) and Ir(18*h*) has four another Ir(18*h*) nearest neighbors.

The remaining atoms: Ir(3*b*) and Ce(6*c*) form a layer that is similar to Ir(6*c*)-Ce(3*a*) plane: Ir(3*b*) are situated between the two metallic planes, just like Ir(6*c*), and form a tetrahedron-like structure with Ir(18*h*) (Ir(18*h*)-Ir(3*b*) distance is equal to 2.68 Å, so it is only 0.04 Å bigger than the Ir(18*h*)-Ir(18*h*) distance). The Ce(6*c*) atoms are moved from the in-plane position closer to the metallic plane, such that they are above the center of a hexagon, consisting of its 6 nearest neighbors Ir(18*h*).

Figure 3 presents the unit cell volume (V) vs. covalent radius of the rare-earth metal (*RE*) for 6 *RE*Ir_3 compounds: $LaIr_3$[18], $CeIr_3$[3,4,6], $PrIr_3$[19], $NdIr_3$[4] and $GdIr_3$[4]. *RE*Ir_3 compounds for rare earths heavier than Gd have not been reported. As expected, the volume increases monotonically with an increase in the covalent radius of the RE^{+3} metal. The trend is linear, except for Ce, for which the unit cell volume is much smaller and comparable with the unit cell volume of $GdIr_3$. This clearly suggests that the Ce oxidation state in $CeIr_3$ is not purely +3, but intermediate between +3 and +4.

Figure 4 presents the results of the XPS investigations of the Ce 3*d* core level spectrum recorded for the sputter-cleaned $CeIr_3$ sample. Due to spin-orbit interactions there are two Ce 3*d* photoemission lines, attributed to the $3d_{5/2}$ and $3d_{3/2}$ components. The splitting in energy between the $3d_{5/2}$ and $3d_{3/2}$ lines is 18.6 eV, while the peaks' intensity ratio $3d_{5/2}/3d_{3/2}$ is 3/2[20–22]. The recorded spectrum was deconvoluted into six peaks, grouped into three doublets corresponding to the $3d^9 4f^0$, $3d^9 4f^1$ and $3d^9 4f^2$ states. The doublet with peaks at 915.5 eV and 896.9 eV is attributed to the $3d^9 4f^0$ state, the doublet at 904.6 eV and 886.0 eV is attributed to the $3d^9 4f^1$ state, while the peaks at 900.3 eV and 881.7 eV are attributed to the $3d^9 4f^2$ state of Ce [10,20–27]. It is well known that the main photoemission lines originating from trivalent cerium are $3d^9 4f^1$, while the presence of $3d^9 4f^0$ peaks indicates that the valence of cerium is larger than 3+[20,21]. Following Refs.[28,29], the mean occupation of the Ce ion ground state can be estimated by comparing the intensity of the latter peak to the sum of intensities of all the components to the Ce 3*d* spectrum. In the case of $CeIr_3$, the ratio $I(f^0)/[I(f^0) + I(f^1) + I(f^2)]$ leads to the effective occupancy of the $4f^0$ level to be 0.95 at room temperature. In turn, on the basis of the Gunnarsson and Schonhammer theory[28,29], the hybridization energy can be determined from the ratio $I(f^2)/[I(f^0) + I(f^1) + I(f^2)]$ that yields for $CeIr_3$ a value of 200 meV. Both the reduced occupancy of the 4*f* state at 300 K and the large strength of the hybridization between the Ce 4*f* electrons and conduction electrons (mostly the 5*d* electrons of Ir, see below), manifest the strongly intermediate valence character of the Ce ions in this material.

The inset of **Figure 5** shows the normal-state magnetic susceptibility data taken over the range 3-300 K in an applied magnetic field of 0.1 T. Above about 50 K, $\chi(T)$ is weakly temperature dependent and its magnitude is small, with a small increase on approaching room temperature. These features are typical for Ce-based intermetallics with valence fluctuations. The pronounced tail seen at low temperatures can be attributed to the presence in the specimen studied of a small amount of magnetic impurities. These could be cerium oxides and/or uncompensated Ce^{+3} ions located on the sample surface or between crystalline grains, as is often observed in intermediate valence materials. Accordingly, the experimental χ(T) data can be described by the formula

$$\chi(T) = \chi_{ICF}(T) + \chi_{imp}(T) + \chi_0 \qquad (1)$$

were χ_{ICF}(T) is the susceptibility given by the inter-configuration fluctuation model (ICF) of intermediate valency[30], χ_{imp}(T) is the Curie-Weiss impurity contribution, assumed to have the form $\chi_{imp}(T) = C_{imp}/(T-\theta_{imp})$, and χ_0 represents temperature independent contributions, e.g. core-electron diamagnetism, conduction-electron paramagnetism and Van Vleck paramagnetism. In the scope of the ICF model the susceptibility of a Ce-based compound with a nonmagnetic $4f^0$ ground state configuration and a magnetic $4f^1$ excited state configuration is represented by

$$\chi_{ICF}(T) = \frac{N\mu_{eff}^2\left[1-\nu(T)\right]}{3k_B\left(T+T_{sf}\right)} \qquad (2)$$

where N and k_B are the Avogadro's number and the Boltzmann constant, respectively, $\mu_{eff} = 2.54\ \mu_B$ is the effective magnetic moment of the exited $4f^1$ state, T_{sf} is the spin fluctuation temperature and the factor $1-\upsilon(T)$ stands for an effective thermal population of the excited state, where

$$\upsilon(T) = \frac{1}{1+6\exp\left[-E_{ex}/k_B\left(T+T_{sf}\right)\right]} \qquad (3)$$

with E_{ex} being an energy gap between the ground and excited states.

The least-squares fit of the experimental data to Eq. 3 yielded the following parameters: T_{sf} = 223 K, E_{ex} = 260 meV, C_{imp} = 0.004 emu K mol^{-1}, χ_{imp} = -3 K and $\chi_0 = 5.5 \times 10^{-5}$ emu mol^{-1}. The calculated $\chi(T)$ is represented in the inset of **Figure 5** by a solid line. The large magnitude of E_{ex}

clearly indicates that the excited $4f^1$ configuration in $CeIr_3$ is quite distant from the nonmagnetic $4f^0$ ground state. In consequence, the effective population of the magnetic $4f^1$ level, which is zero at zero Kelvin, hardly changes with increasing temperature reaching a value of only 0.02 at 300 K. This finding naturally explains a Pauli-like character of $\chi(T)$ below room temperature.

Attributing the low temperature tail in $\chi(T)$ to stable Ce^{+3} ions only, the impurity concentration ($n = C_{imp}/C_{Ce3+}$ where $C_{Ce3+} = \mu_{eff}^2/8$) is estimated to be only 0.5 at% Ce^{+3} ions per mol, i.e. well below the detection limit of standard X-ray diffraction.

The magnetic characterization of the superconducting properties of $CeIr_3$ is shown in the main panel of **Figure 5**. Both zero-field-cooled (ZFC) and field-cooled (FC) temperature-dependent volume magnetic susceptibility measurements, χ_V = dM/dH where M is the magnetization and H is the applied field, were performed under an applied magnetic field of 20 Oe. The bifurcation of the ZFC and FC magnetic susceptibilities indicates the transition into the superconducting state, which is in agreement with reported data[5,6,16,31]. It can be seen that for the ZFC signal, the transition is slightly broadened and reaches saturation at lower temperature. When corrected for the demagnetization effect, N = 0.52 (estimated from the M(H) fit discussed in the following section), at the lowest temperature T = 1.67 K, the diamagnetic signal exceeds the expected $\chi_V = -1/4\pi(1-N)$ value, indicating a full Meissner state. The FC signal is much weaker, likely caused by strong flux pinning in our $CeIr_3$ sample. The superconducting critical temperature (T_c) was estimated as the intersection between two lines: the first one is an extrapolation of the normal state χ_V to lower temperature and the second is the steepest slope line of the superconducting signal[32]. The T_c for $CeIr_3$ is 2.5 K and is slightly lower than reported in the literature[5,6,16,31]. Defining the critical temperature as the onset of the transition to the superconducting state $T_{c\ onset}$ is about 2.7 K. It is worth noting that a sample with nominal composition $CeIr_3$ did not show superconductivity, and that two-step superconductivity is observed for nominal $Ce_{1.05}Ir_3$. This suggests that superconductivity in this system is very sensitive to the chemical composition.

In **Figure 6(a)**, the field-dependent magnetization curves $M_V(H)$ for $CeIr_3$ measured at different temperatures are shown. Assuming that a linear response to an applied magnetic field indicates a full Meissner effect, the demagnetization factor N = 0.52 was obtained. The N value is consistent with the sample shape with respect to the magnetic field. The inset shows the full magnetization versus applied magnetic field loop collected in the superconducting state at 2 K. It is evident that $CeIr_3$ exhibits conventional type-II superconductivity. The irreversible field (H_{Irr}) estimated from the plotted curve is 4.5 kOe at 2 K and for fields $H > H_{Irr}$, vortices are unpinned. The linear fit (M_{fit}) to the initial slope in magnetization curves was used to construct the M_V-M_{fit} and plotted as a function of the applied magnetic field (see **Figure 6(b)**). The field where there is the first deviation from a linear response of the magnetization curve (black dashed line) is the lower critical field, H_{c1}, at each temperature. At T = 1.7 K, H^*_{c1} is 50 Oe and decreases monotonically with an increase in temperature, to 23 Oe at T = 2.3 K. The H^*_{c1} values with the corresponding temperatures are shown in **Figure 6(c)**. As expected, H^*_{c1} varies as a function of T^2 in accordance with Ginzburg-Landau (GL) theory:

$$H^*_{c1}(T) = H^*_{c1}(0)\left[1 - \left(\frac{T}{T_c}\right)^2\right], \quad (4)$$

where $H^*_{c1}(0)$ is the lower critical field at 0 K and T_c is the superconducting critical temperature. The quadratic equation fits the data well and, for $CeIr_3$, H^*_{c1} at 0 K is estimated to be 83(3) Oe. Correcting for the demagnetization factor (N = 0.52), the lower critical field at 0 K is calculated to be $H_{c1}(0)$ = 173 Oe (17.3 mT). This value is larger than that reported for the $CeIr_3$ single crystal ($H_{c1}(0)$ = 51 Oe)[6].

The temperature dependence of the electrical resistivity for $CeIr_3$ between 1.85 and 300 K in zero magnetic field is presented in the main panel of **Figure 7.** The overall $\rho(T)$ behavior is typical of intermetallic compounds[18,33,34] – at low temperatures a residual resistivity (ρ_0) is observed and the high temperature data show tendency towards saturation that would be expected as the charge carrier mean-free path becomes comparable to the interatomic distances[35–37]. Similar behavior has been

reported for other Ir-based superconductors e.g., $CaIr_2$[38] , $LaIr_3$[18], $TaIr_2Ge_2$[33] and La_7Ir_3[39]. The other plausible scenario assumes s-d Mott scattering[40–42]. The residual resistivity ratio (ρ(300 K)/ρ(10 K) = 1.7) is found to be rather small, which suggests that the resistivity is dominated by disorder in the polycrystalline sample. At low temperatures, the resistivity of $CeIr_3$ indicates a superconducting transition at 2.75 K, where T_c is taken as 50% of the resistivity drop. The slightly higher critical temperature value obtained in the resistivity measurement is likely due to the influence of surface superconductivity emerging in each cross-sectional area of the sample. The inset of **Figure 7** shows the magnetic field-dependent resistivity of $CeIr_3$ around the transition. As expected, the superconducting transition becomes broader and the T_c shifts to lower temperature as the applied magnetic field is increased. These data were used to extract the upper critical field ($\mu_0 H_{c2}$), taken as the midpoint of the resistivity transition at each applied field. The upper critical field $\mu_0 H_{c2}(T)$ of $CeIr_3$ is presented in **Figure 9** and will be discussed further.

In order to characterize the thermodynamic transition, specific heat measurements were conducted on a flat polished sample. **Figure 8(a)** presents a closer view of the transition temperature under zero magnetic field. The sharp anomaly displayed in the specific heat data confirms bulk superconductivity in $CeIr_3$. In order to extract the superconducting transition temperature and the value of the specific heat jump, we used a linear approximation of the data just above and below the transition. The corresponding graphical equal-area construction (entropy conserving) with the vertical line located at the transition temperature T_c = 2.46 K is shown by solid blue lines in **Figure 8(a)** and is slightly lower than the value obtained from resistivity data (as described above) and comparable with the T_c estimated from the magnetic susceptibility measurement. The specific heat jump is found to be about $\Delta C/T_c$ = 31.2 mJ $mol^{-1}K^{-2}$. In part (b) of the same figure, the normal-state specific heat of $CeIr_3$ is presented under a magnetic field of $\mu_0 H$ = 2 T. The data plotted as C_p/T versus T^2 can be fitted using the formula $C_p/T = \gamma + \beta T^2$, where γT and βT^3 are the electronic specific heat coefficient and phonon contribution, respectively. A linear least-squares fit yields the

Sommerfeld coefficient γ = 25.1(3) mJ mol^{-1}K^{-2} and β = 2.72(6) mJ mol^{-1}K^{-4}. In a simple Debye model for the phonon contribution, the β coefficient is related to the Debye temperature Θ_D through

$$\Theta_D = \left(\frac{12\pi^4}{5\beta} nR\right)^{1/3} \quad (5)$$

where R = 8.314 J mol^{-1}K^{-1} and n = 4 for $CeIr_3$. The calculated Debye temperature is 142(1) K, which is very close to the value obtained for $CeIr_3$ single crystals[6]. The specific heat anomaly observed at the superconducting transition is usually normalized as $\Delta C/\gamma T_c$. Using the value of $\Delta C/T_c$ = 31.2 mJ mol^{-1}K^{-2} and γ = 25.1(3) mJ mol^{-1}K^{-2}, we obtained $\Delta C/\gamma T_c$ = 1.24. The calculated value is slightly lower than the BCS value of 1.43, suggesting that $CeIr_3$ is a weakly coupled superconductor, however the value is very close to that for $LaIr_3$[18] ($\Delta C/\gamma T_c$ = 1.22).

Knowing the Debye temperature, the electron-phonon coupling constant, $\lambda_{e\text{-}p}$, can be estimated from the inverted McMillan equation[43]

$$\lambda_{e-p} = \frac{1.04 + \mu^* \ln(\Theta_D/1.45T_c)}{(1 - 0.62\,\mu^*)\ln(\Theta_D/1.45T_c) - 1.04} \quad (6)$$

where μ^* is the repulsive screened Coulomb constant, typically taken as μ^* = 0.13 for many intermetallic superconductors[6,33,44–46]. Using the Debye temperature Θ_D = 142(1) K and T_c = 2.46 K (from the specific heat measurements), we obtain $\lambda_{e\text{-}p}$ = 0.65, which suggests weak electron-phonon coupling behavior. In addition, for non-interacting particles, the electronic specific heat coefficient is proportional to the density of states at the Fermi energy $N(E_F)$. Using the relation

$$N(E_F) = \frac{3\gamma}{\pi^2 k_B^2 (1 + \lambda_{e-p})}, \quad (7)$$

where k_B is the Boltzmann constant, $N(E_F)$ is calculated to be 6.5 states eV^{-1} per formula unit for $CeIr_3$.

Figure 8(c) shows the specific heat data plotted as C_p/T versus T in various magnetic fields. The vertical solid lines present the midpoints of the superconducting transitions for each applied field from 0 T to 2 T. With increasing magnetic field, the size of the specific heat jump becomes

smaller and shifts to lower temperatures. Using the transition temperature estimated at different magnetic fields, we can calculate the upper critical field $\mu_0 H_{c2}(T)$. Determination of the upper critical field $\mu_0 H_{c2}$ via resistivity (green squares) and heat capacity (blue circles) measurements is shown in **Figure 9**. For a single-band type-II BCS superconductor, the orbital upper critical field at 0 K can be estimated from the Werthamer-Helfand-Hohenberg (WHH) expression[47,48]

$$\mu_0 H_{c2}(0) = -AT_c \left.\frac{d\mu_0 H_{c2}}{dT}\right|_{T=T_c} \quad (8)$$

where A is the purity factor given by 0.693 for the dirty and 0.73 for the clean limit. Although the data points are shifted, the $d\mu_0 H_{c2}/dT$ slope determined from the $\rho(T)$ data and $C_p(T)$ data are almost identical $d\mu_0 H_{c2}/dT$ = -2.01(2) T/K and -2.08(6) T/K, respectively. Taking T_c = 2.46 K, for $CeIr_3$ we estimate $\mu_0 H_{c2}(0)$ = 3.5 T in the dirty limit and $\mu_0 H_{c2}(0)$ = 3.7 T in the clean limit. The value of the upper critical field is smaller than the Pauli limiting field for weak electron-phonon coupling within the BCS theory[49,50] $H_{c2}^p(0) = 1.85\, T_c$ which for T_c = 2.46 K gives $H_{c2}^p(0) = 4.6$ T for $CeIr_3$.

Assuming that the upper critical field is purely orbital, the superconducting coherence length is calculated to be ξ_{GL}= 97 Å, using the Ginzburg-Landau formula[51] $H_{c2} = \Phi_0/2\pi\xi_{GL}^2$ where Φ_0 = hc/2e is the quantum flux. Similarly, from the relation

$$H_{c1} = \frac{\Phi_0}{4\pi\lambda_{GL}^2}\ln\frac{\lambda_{GL}}{\xi_{GL}}, \quad (9)$$

we find the superconducting penetration depth λ_{GL} = 1640 Å for $CeIr_3$. The Ginzburg-Landau parameter $\kappa_{GL} = \lambda_{GL}/\xi_{GL}$ can then be estimated as κ_{GL} = 17, supporting the type-II nature of the superconductivity. Finally, the thermodynamic critical field can be obtained from κ_{GL}, H_{c1} and H_{c2} using the formula

$$H_{c1}H_{c2} = H_c^2 \ln \kappa_{GL} \quad (10)$$

yielding $\mu_0 H_c$ = 147 mT. A summary of all the measured and calculated superconducting parameters determined here for $CeIr_3$ are gathered in **Table 3**.

In the calculations, the electronic structure for $CeIr_3$ is compared to that of $LaIr_3$[18], which is an isostructural superconductor with an unoccupied La 4*f* shell. The densities of states (DOS) of $CeIr_3$ calculated without (labeled as no U) and with (labeled as +U) electron-electron interactions, together with the DOS of $LaIr_3$ are presented in **Figure 10**. The partial densities of states are shown in **Figure 11**, and the Fermi surface and electronic dispersion relations of $CeIr_3$ are shown in **Figure 12**. The values of the DOS at the Fermi level (E_F) and the occupancy of electronic orbitals are presented in **Table 4** and **Table 5** for $CeIr_3$ and $LaIr_3$, respectively, while the calculated Sommerfeld coefficients and the electron-phonon coupling parameters are given in **Table 6**.

Cerium atoms ($[Xe]4f^15d^16s^2$) contribute four, while iridium ($[Xe]5d^76s^2$) atoms contribute nine valence electrons to the electronic system. Our spin-polarized calculations converged to a non-magnetic state, for both types of calculations: with U and without U. This is seen in the DOS of $CeIr_3$ in **Figure 10**, where the spin-up and spin-down parts are practically the same. The main valence band block (from -10 eV to E_F) consists mainly of Ir 5*d* states, with a small fraction of *d*-states of Ce and 6*s*-states of Ir, with the latter in the lower energy part. 4*f* electronic states of Ce form a large DOS peak, seen above the Fermi level, where also smaller contributions from unoccupied 5*d*-states of Ce and Ir are visible.

Evidently, the inclusion of Coulomb repulsion (calculations including U) shifts the 4*f*-states further above the Fermi level, which strongly reduces the calculated occupancy of the 4*f*-orbitals of Ce. Total and partial densities of states at the Fermi level are collected in **Table 4**. The dominating contribution to DOS(E_F) comes from 5*d* states of Ir atoms, as also can be deduced from **Figure 11.** Among the Ir atoms, the largest partial DOS(E_F) is found on Ir(6*c*) atoms, which form the Kagome-like 2D lattice with Ce(3*a*) in the crystal structure. However, since there are three times more Ir(18*h*), in comparison with Ir(6*c*), the total contribution from the Ir(18*h*) sublattice to the density of states at the Fermi level is the largest one. The overall domination of Ir 5*d* states at the Fermi surface strongly suggests that the superconductivity of $CeIr_3$ is mediated by the *d*-states of Ir atoms. This situation is

similar to what was previously found for $LaIr_3$ (which has T_c=3.32 K, slightly larger than that of $CeIr_3$), for which the *d*-states of Ir were concluded to be the most important for superconductivity[18]. By comparing the densities of states of these two systems, plotted in **Figure 10(b)** and **10(c)**, one can see that the overall shape of the DOS function of $CeIr_3$ below the Fermi level is similar to the one of $LaIr_3$, which means that states from Ir are hybridized with Ce/La in a similar way. Thus, the main difference between these systems comes from the additional valence electron provided by the cerium atom. As a consequence, the Fermi level is shifted to higher energies, towards the DOS minimum seen just above E_F, making the DOS(E_F) value smaller in $CeIr_3$. This is correlated with its smaller superconducting critical temperature (2.46 K in $CeIr_3$ compared to 3.32 K in $LaIr_3$).

Table 4 also includes the orbital occupation numbers, computed by integrating the angular momentum decomposed partial densities of states inside the atomic spheres (R_{Ce} = 2.9 a_B, R_{Ir} = 2.48 a_B, a_B is the Bohr radius). Due to hybridization, we observe an *s*-*p* transfer of electronic states for all of the atoms, and importantly, strong reduction of the 4*f* orbital occupation, to about 0.2. These results, together with the DOS and dispersion relation plots, show rather strong hybridization of the Ce 4*f* states, giving rise to the itinerant picture of the 4*f* electrons in that material. Qualitatively, such a low occupation of the 4*f* shell confirms that Ce ions in $CeIr_3$ are closer to the Ce^{4+} ($4f^0$) configuration, than to the magnetic Ce^{3+} ($4f^1$) state, in agreement with experimental findings. Concerning the valence state of the Ce atoms, our DFT 4*f* occupation would correspond to 20% of Ce^{3+} and 80 % of Ce^{4+} valence states, giving the average valence of 3.2. This is not far from the value of 3.38, suggested in Ref.[16] as well as from 3.30, assumed to be the highest possible valence for the $4f_0$ state in an intermetallic compound[52].

To complete the discussion of the electronic band structure, **Figure 12** presents the electronic dispersion relations and Fermi surface (FS) of $CeIr_3$. As our calculation resulted in a non-magnetic ground state, only one spin direction is presented. In the GGA calculations, four bands cross the Fermi level, building up four pieces of the FS. When U is included, one piece consisting of a small

Γ-centered pocket (**Figure 12(a)**), associated with the band colored in red in **Figure 12(i)**, disappears. The hole-like piece of the FS (**Figure 12(b)**) consists of a Γ-centered pocket and six pockets around the T-point, which become disconnected once the Coulomb repulsion is turned on (**Figure 12(f)**). This piece of the FS is built up from the band plotted in blue in **Figure 12(i) and 12(j)**. The third piece of the FS (**Figure 12(c)**) is cylinder-like in shape, with the symmetry axis around the trigonal direction, which becomes more pronounced when the U repulsion is included. This quasi-2D behavior of this part of the FS may be connected to the sequence of metallic Ir layers perpendicular to the trigonal axis. The associated band (plotted in purple in **Figure 12(i) and 12(j)**) is almost linear in in-plane directions (T-C-C'-T). The last, electron-like piece of the FS (**Figure 12(d)** and **12h)**) consists of six small pockets around the L-points, which are associated with the orange band in **Figure 12(i)** and **12(j)**, and cross E_F at two non-high symmetry points in the Y-L direction. In conclusion, the Fermi surface is rather complex, $CeIr_3$ is a multi-band superconductor, and in large areas of reciprocal space, a steep and quasi-linear character of the dispersion is observed, which is responsible for a relatively small total density of states in this compound. It is worth noting that the FS of the sister compound $LaIr_3$ (see Ref.[18]) consists of three analogous parts, however due to its different Fermi level position, only the cylinder-like part (here presented in **Figure 12(c) and (g)**) looks similar.

Finally, we compare the theoretical density of states with the heat capacity measurements. The GGA+U value of the Sommerfeld coefficient γ_{GGA+U} = 5.7 mJ $mol^{-1}K^{-2}$ (shown in **Table 6**) is much smaller than the experimental one, γ_{expt} = 25 mJ $mol^{-1}K^{-2}$. This difference cannot be explained by the renormalization due to the electron-phonon interaction only, since that would require having very large λ_{e-p} value, $\lambda_{e-p} = \gamma_{expt}/\gamma_{calc} - 1 = 3.4$, which strongly disagrees with the value obtained using the experimental T_c and the McMillan formula (λ_{e-p} = 0.65). This suggests the presence of an additional renormalization of the electronic specific heat due to electronic interactions, treated in our GGA+U calculations in an approximate way. It is also possible that the SIC method used to deal

with correlated *f*-electrons leads to too strong reduction of the presence of 4*f* states near the Fermi level. In calculations without U the DOS(E_F) is larger, equal to 4.38 ev^{-1} per f.u, which leads to a larger γ_{calc} = 10.2 (mJ mol^{-1} K^{-2}) and λ_{e-p} = 1.5, so still twice as large as expected from the McMillan formula. Calculations done using the AMF double-counting method[15] resulted in a γ_{calc} much closer to the experimental value, however, as mentioned above, this method predicted an erroneous magnetic ground state of the system. This reflects the fact that density functional calculations usually face problems with cerium compounds.

For the case of $LaIr_3$, on the other hand, the computed "bare" value of the Sommerfeld coefficient γ_{calc} = 9.2 (mJ $mol^{-1}K^{-2}$) is very close to the experimental γ_{expt} = 11.5 (mJ $mol^{-1}K^{-2}$)[18] leaving room only for a small renormalization parameter λ_{e-p} = 0.25. This is smaller than expected from the magnitude of T_c (λ_{e-p} = 0.55), however the disagreement is not as substantial as for the Ce-containing case.

Conclusion

In summary, we have synthesized and studied the physical properties of polycrystalline $CeIr_3$. Single crystal diffraction and a LeBail refinement of the powder X-ray diffraction data confirm the rhombohedral structure in centrosymmetric space group *R-3m* (No. 166) with lattice cell parameters *a* = 5.2945(1) Å, *c* = 26.219(1) Å (at room temperature) in agreement with the literature. The calculated unit cell volume for $CeIr_3$ does not follow the trend expected for rare earth based compounds and suggests that the Ce oxidation state in $CeIr_3$ is not +3. This was proven through our room temperature XPS and magnetic susceptibility studies. The normal state magnetic susceptibility was fitted by using the inter-configuration fluctuation model (ICF) of intermediate valency.

Temperature-dependent magnetic susceptibility, resistivity and heat capacity measurements confirm bulk superconductivity with T_c = 2.46 K. Analysis of the specific-heat data reveal that $CeIr_3$ is a moderately correlated superconductor (λ_{e-p} = 0.65). Detailed analysis of field dependent

magnetization allowed us to estimate the lower critical field at T= 0 K (17.3 mT). Resistivity and heat capacity measurements, performed under various magnetic fields and below T_c, give the upper critical field at 0 K of about 3.5 T, which is below the Pauli limit for $CeIr_3$ $H_{c2}^{p}(0) = 4.6$ T. Our values are close to the superconducting parameters refined by Sato, et. al on a $CeIr_3$ crystal obtained by the Czochralski method[6].

Our band structure calculations confirm the non-magnetic ground state of this compound, with a small occupation of the Ce 4*f* shell. The computed Fermi surface indicates a multi-band character for this compound, with the dominating contribution to DOS(E_F) coming from 5*d* states of Ir atoms. The overall domination of Iridium 5*d* states at the Fermi surface strongly suggests that $CeIr_3$ is indeed an Ir 5*d*-band superconductor and that 5*d* electrons play the dominant role in the superconductivity; a similar situation is observed[16] for $CeRu_2$ and $LaIr_3$. On the other hand, the enhanced Sommerfeld coefficient γ_{expt} of $CeIr_3$ compared to that of $LaIr_3$, and the disagreement between the computed and measured γ values show that the hybridized 4*f* electronic states of Ce in $CeIr_3$ have a subtle impact on the physical properties

Acknowledgements

This work was supported by the Ministry of Science and Higher Education (Poland) under project DI2016 020546 ("Diamentowy Grant"). Research performed at the AGH-UST was supported by the National Science Center (Poland), project No. 2017/26/E/ST3/00119. The materials synthesis and powder X-ray diffraction work at Princeton University was supported by the US Department of Energy, Division of Basic Energy Sciences, grant DE-FG02-98ER45706.

Figures

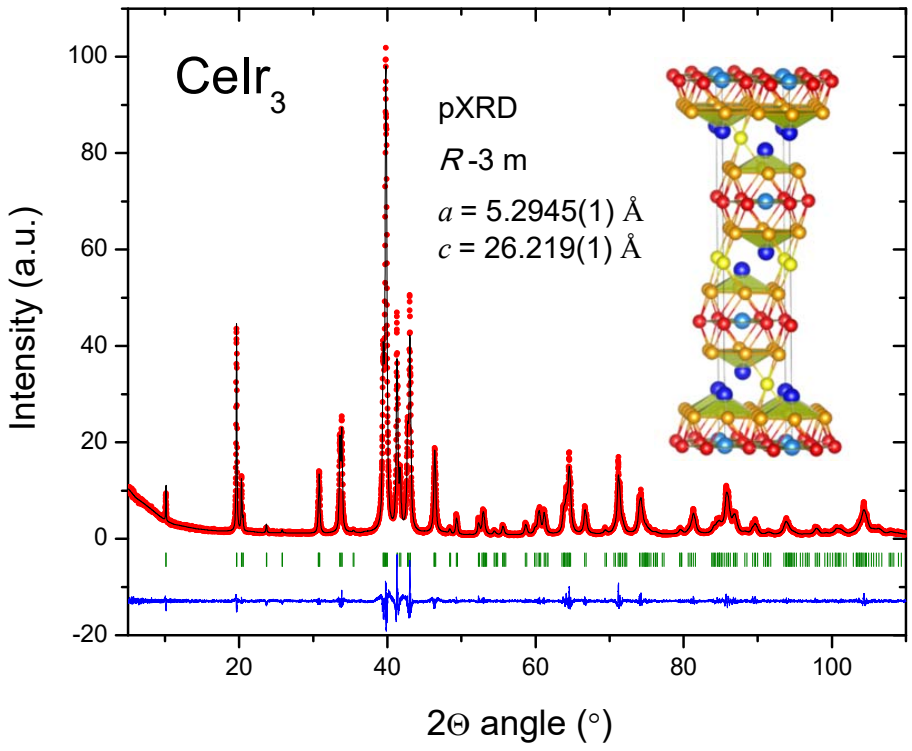

Fig. 1. Powder X-ray diffraction pattern (red points) together with the LeBail refinement profile (black solid line) for $CeIr_3$. The green vertical bars indicate the expected Bragg peak positions. The blue curve is the difference between experimental and model results.

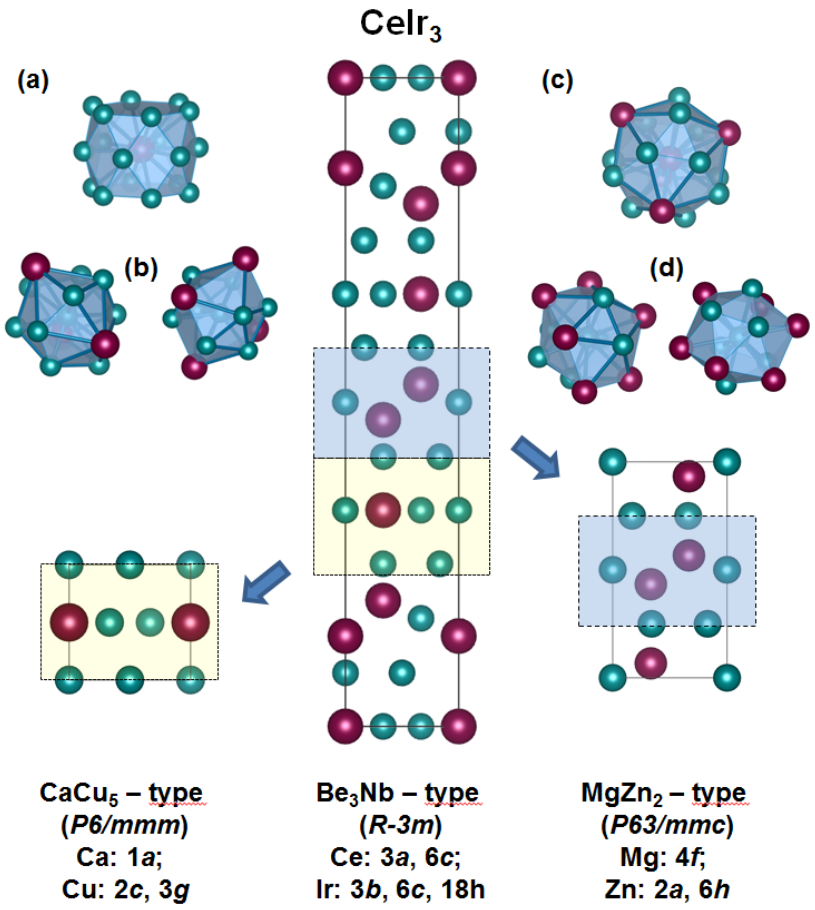

Fig. 2. Crystal structure of $CeIr_3$, with polyhedral and slab layers emphasized. (a) 16 vertex polyhedron with a Ce atom center in $CaCu_5$–type $CeIr_5$, (b) distorted icosahedra with Ir atom centers in $CaCu_5$–type $CeIr_5$, (c) 12 vertex polyhedron with Ce atom center in $MgZn_2$–type $CeIr_2$, (d) distorted icosahedra with Ir atom centers in $MgZn_2$-type $CeIr_2$.

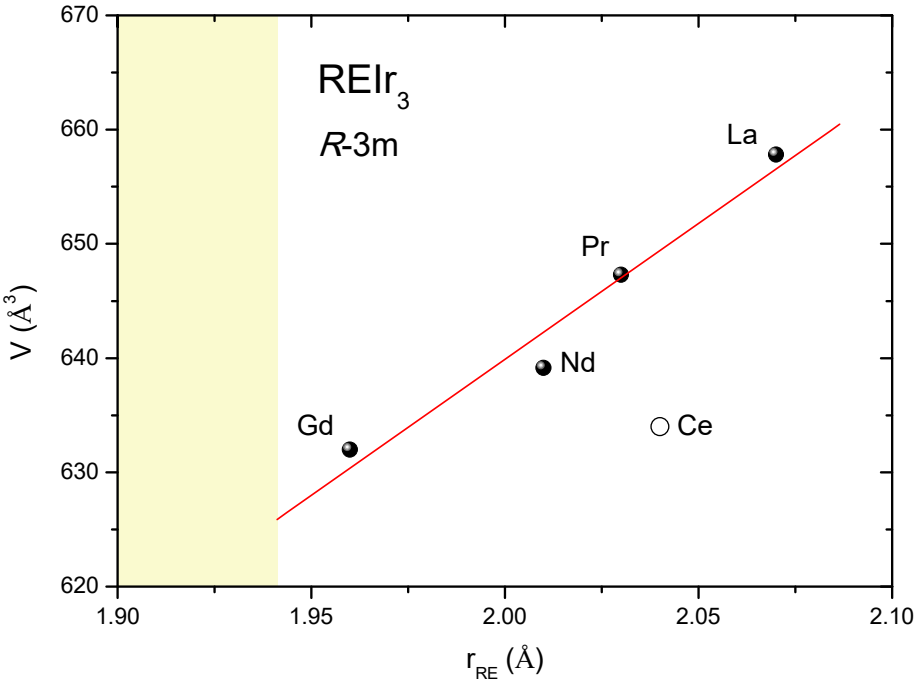

Fig. 3. Unit cell volume (V) vs. covalent radius for $REIr_3$ compounds, where RE is a heavy rare earth metal (La, Ce, Pr, Nd and Gd). The unit cell volume values were taken from references: [4–6,18,19].

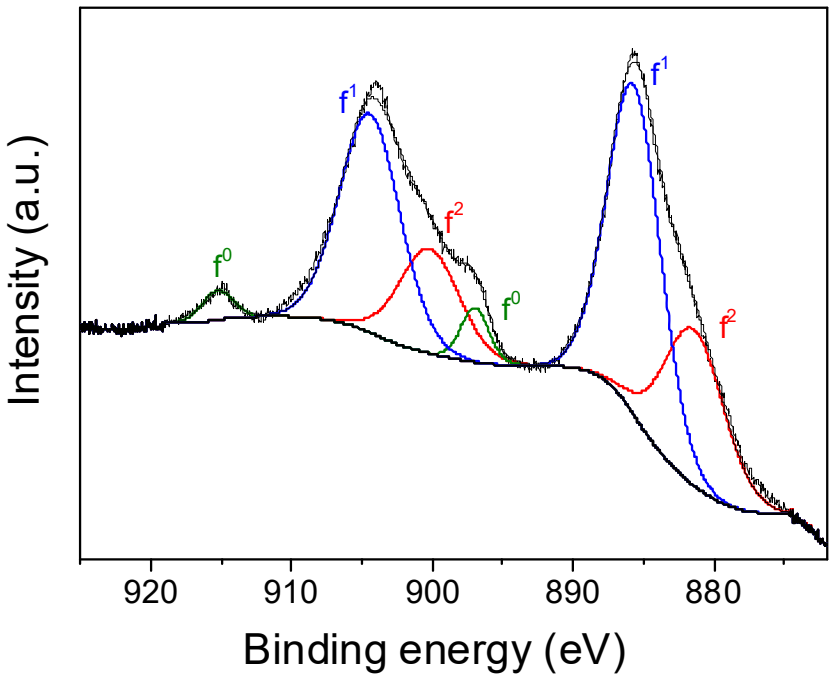

Fig. 4. XPS Ce 3*d* spectrum of a sputter-cleaned $CeIr_3$ sample. f^0 f^1 and f^2 refer to spectral characteristics resulting from electron occupancy in the f orbitals.

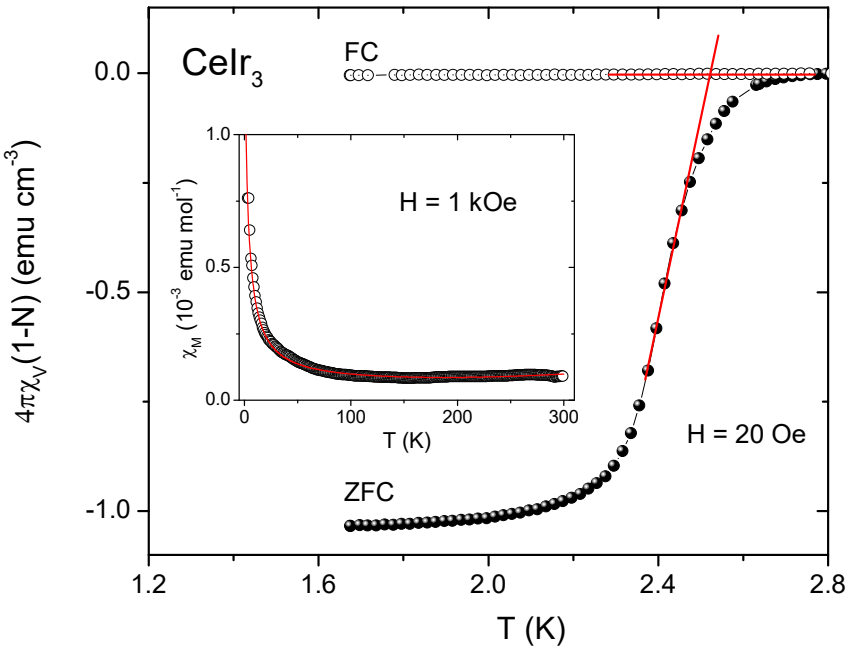

Fig. 5. Main panel: Zero-field-cooled (ZFC) and field-cooled (FC) temperature-dependent volume magnetic susceptibility $\chi_V(T)$ measurements performed under a small applied magnetic field of 20 Oe. Inset shows normal-state magnetic susceptibility vs temperature data over the range 3-300 K in a field of 1000 Oe. Details of the fit (solid line) are explained in the text.

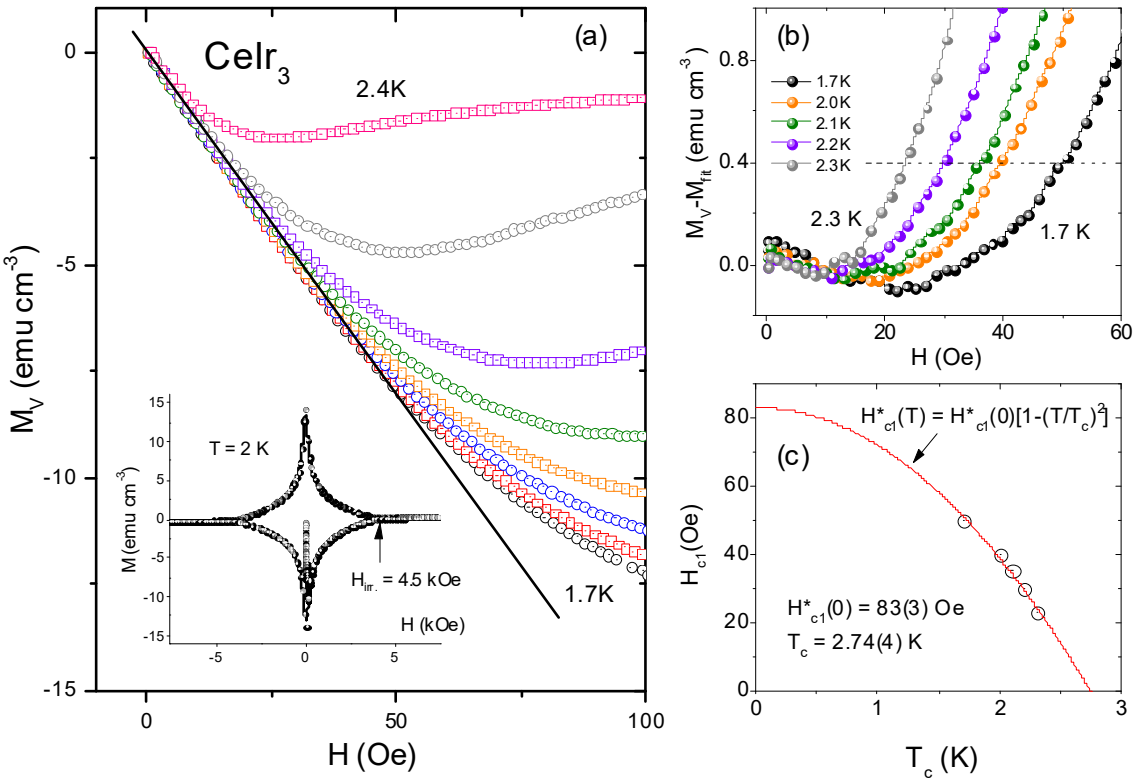

Fig. 6(a): The field-dependent magnetization curves $M_V(H)$ for $CeIr_3$ taken at different temperatures. The inset shows the magnetization hysteresis loop at 2 K. (b) M_V-M_{fit} plotted as a function of applied magnetic field and (c) the H^*_{c1} values with the corresponding temperatures.

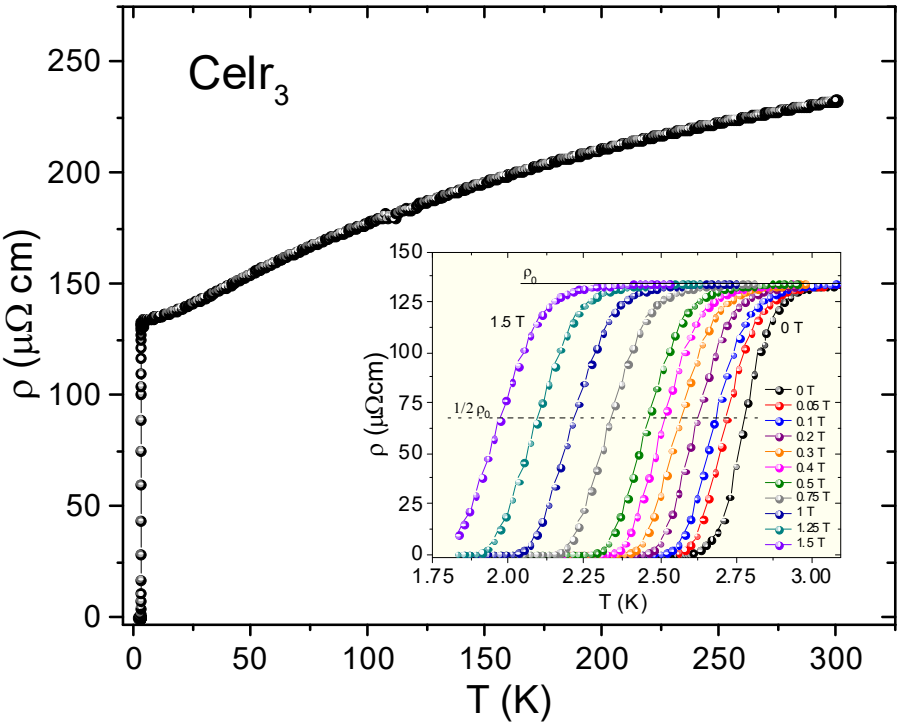

Fig. 7. The temperature dependence of the electrical resistivity for $CeIr_3$ between 1.85 and 300 K in zero magnetic field. Inset: the magnetic field-dependent resistivity of $CeIr_3$ in the vicinity of the superconducting transition.

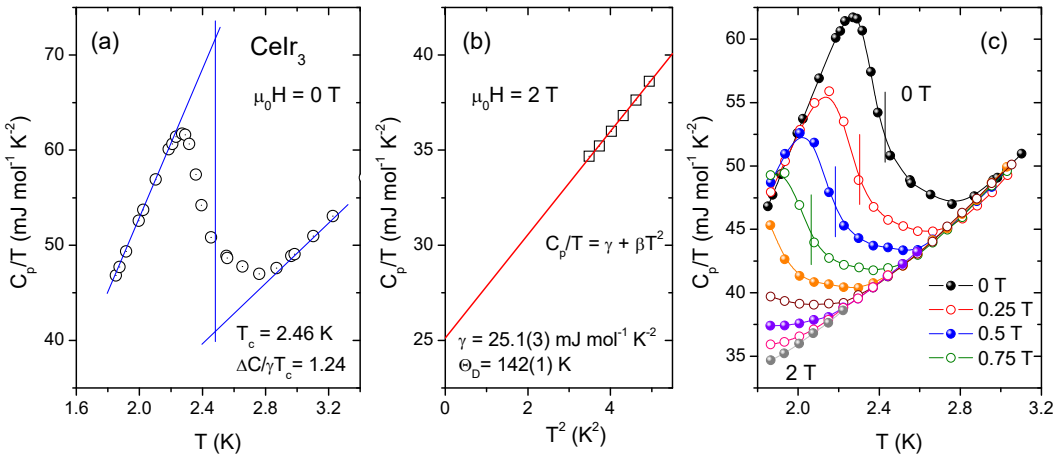

Fig. 8 (a). The specific heat anomaly in zero magnetic field. (b) C_p/T vs T^2 plot under a $\mu_0H = 2T$ magnetic field. The red solid line represents the linear fit of the data. (c) C_p/T vs T under various applied magnetic fields.

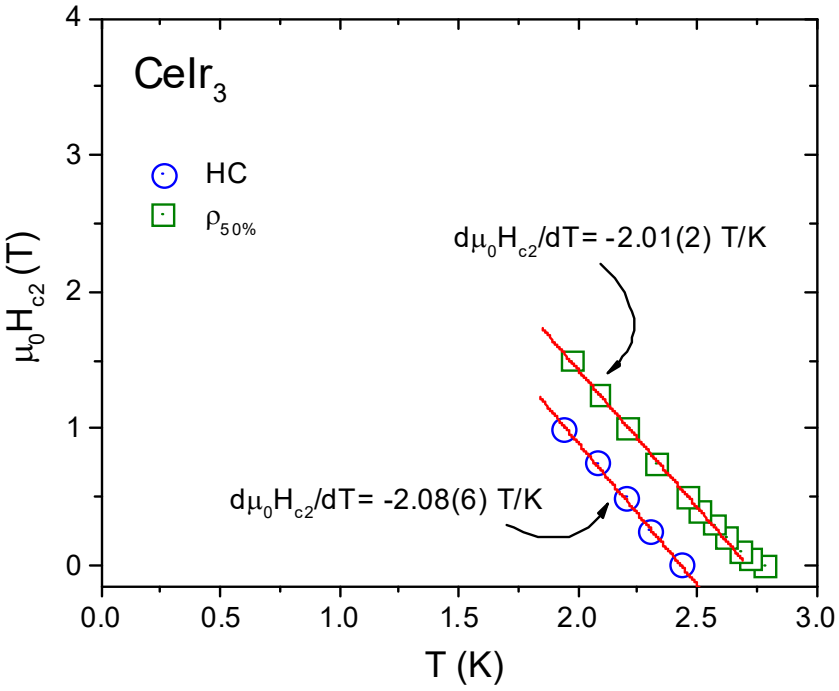

Fig. 9. The temperature dependence of the upper critical field of $CeIr_3$, determined from heat-capacity (blue circles) and electrical resistivity (green squares) measurements.

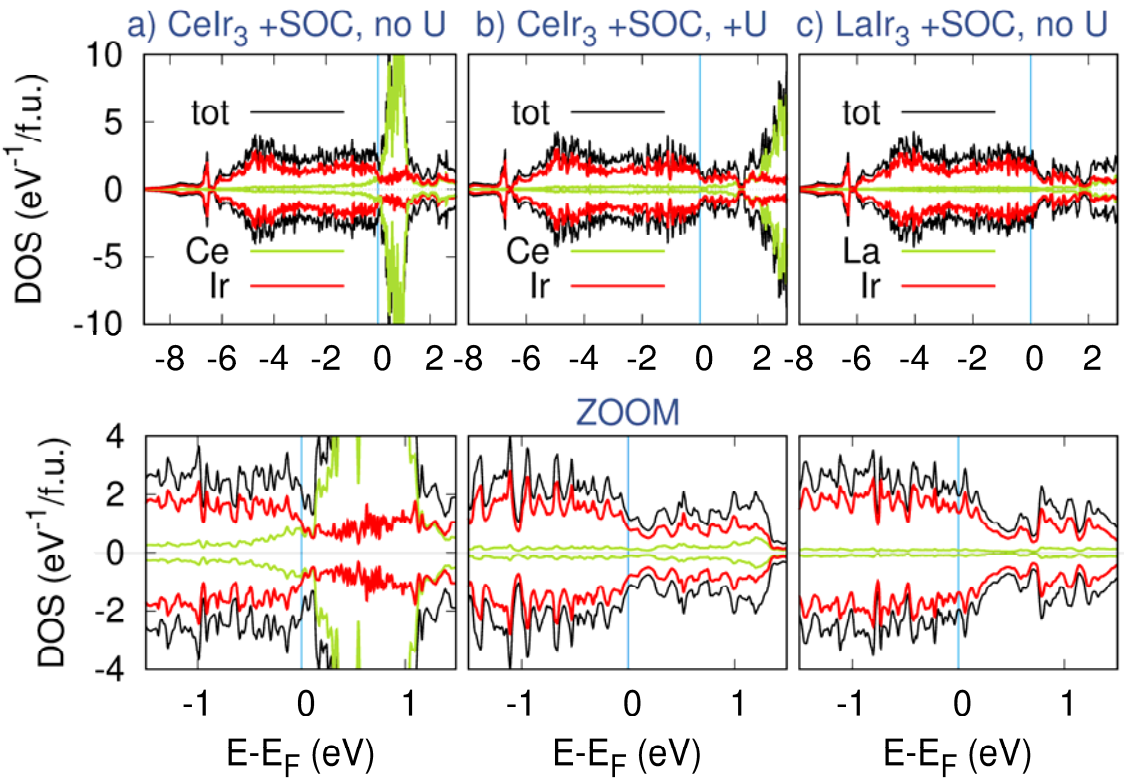

Fig. 10. Density of states of $CeIr_3$ compound calculated with SOC and a) without U, b) with U_{eff} = 5 eV and c) density of states of $LaIr_3$. The main valence band is shown at the top while the DOS in the vicinity of Fermi level is shown at the bottom.

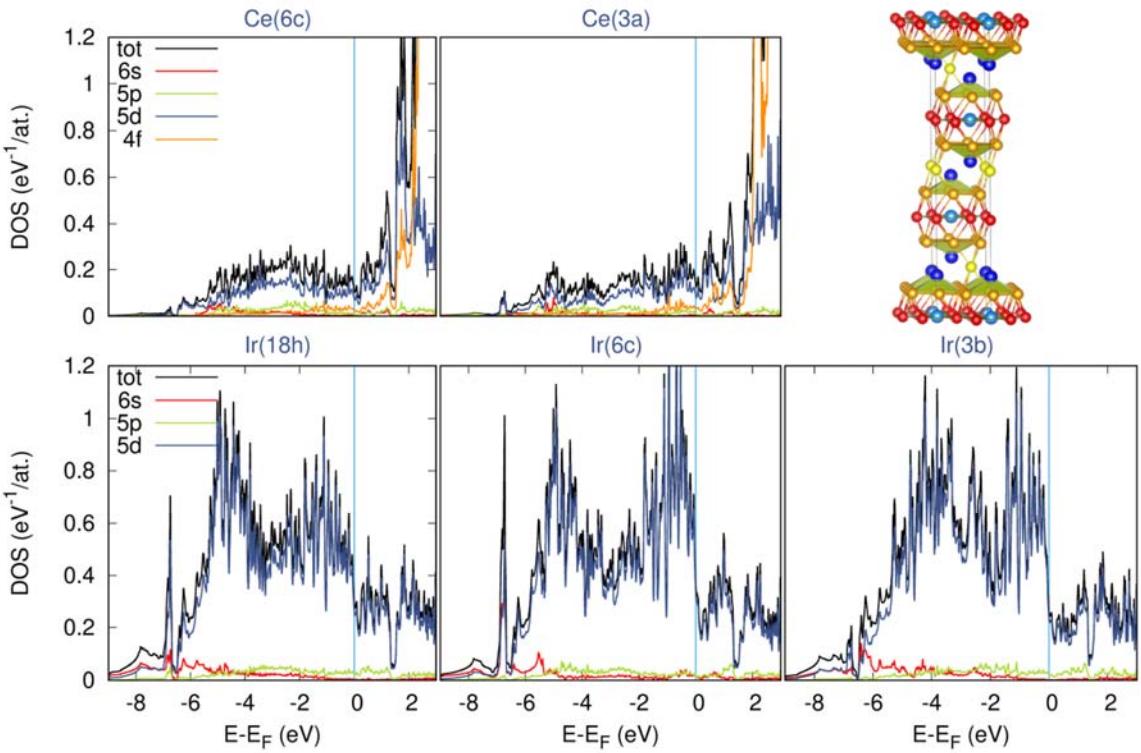

Fig. 11. Partial density of states of $CeIr_3$ coming from all five nonequivalent atoms, calculated with U_{eff} = 5 eV and SOC and the crystal structure of $CeIr_3$: Ce(6c) and Ce(3a) are marked with dark and light blue balls, while the Ir(18h), Ir(6c) and Ir(3b) atoms are marked by orange, red and yellow balls respectively.

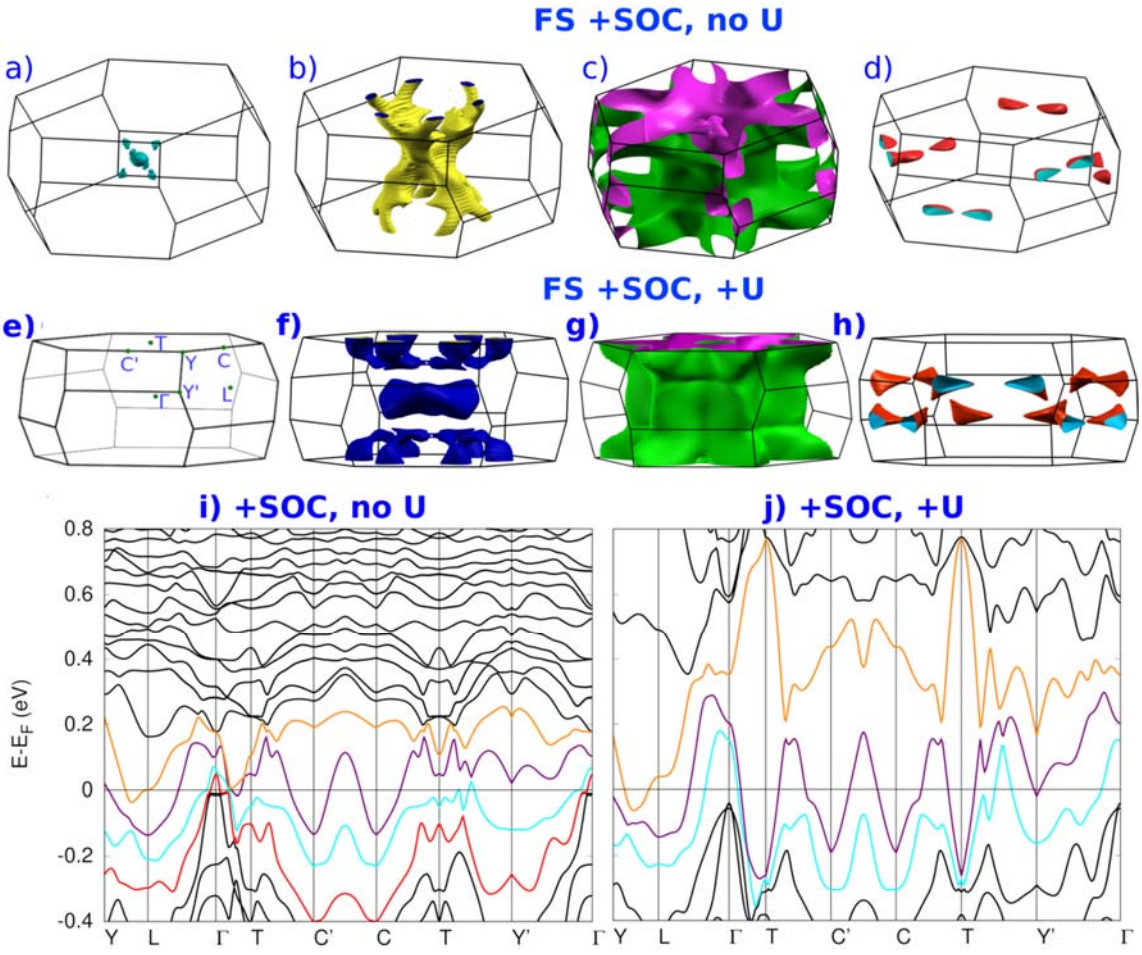

Fig. 12. The Fermi surface of $CeIr_3$ calculated (a-d) without U; (f-h) with U_{eff} = 5 eV; the same for the electronic structure (i) and (j). Panel (e) shows the location of the high-symmetry points. The Fermi surface was plotted using XCrysDen[53]

Table 1. Crystallographic data for $CeIr_3$ at 175(2) K

$CeIr_3$	
F.W. (g/mol);	716.72
Space group; Z	*R-3m* (No.166); 9
Lattice Parameters	a= 5.280 (4) Å c= 26.166 (20) Å
Volume (Å^3)	640 (1)
Absorption Correction	Numerical
Θ range (deg)	2.335 to 33.058
hkl ranges	$-8 \leq h,k \leq 8$ $-39 \leq l \leq 39$
No. reflections; R_{int}	3239; 0.1041
No. independent reflections	347
No. parameters	18
R_1; wR_2 (all I)	0.0558; 0.1185
Goodness of fit	1.000
Diffraction peak and hole (e^-/Å^3)	5.150; -4.140

Table 2. Refined atomic coordinates and equivalent isotropic displacement parameters of $CeIr_3$ (U_{eq} is defined as one-third of the trace of the orthogonalized U_{ij} tensor ($Å^2$))

Atom	Wyck.	Occ.	*x*	*y*	*z*	U_{eq}
Ce1	3*a*	1	0	0	0	0.0052(10)
Ce2	6*c*	1	0	0	0.1395(1)	0.0066(7)
Ir1	3*b*	1	0	0	½	0.0087(7)
Ir2	6*c*	1	0	0	0.3334(1)	0.0094(6)
Ir3	18*h*	1	0.5007(2)	0.4993(2)	0.0824(1)	0.0071(4)

Table 3. Experimental superconducting and normal state parameters of $CeIr_3$

Parameter	**Unit**	**Value**
T_c	K	2.46
$\mu_0 H_{c2}(0)$	T	3.5
$\mu_0 H_{c1}(0)$	mT	17.3
$\mu_0 H_c$	mT	147
$\lambda_{e\text{-}p}$	---	0.65
$\xi_{GL}(0)$	Å	97
$\lambda_{GL}(0)$	Å	1640
κ	---	17
γ	mJ mol^{-1} K^{-2}	25.1(3)
β	mJ mol^{-1} K^{-4}	2.72(6)
Θ_D	K	142(1)
RRR	---	1.7
$\Delta C_p/\gamma T_c$	---	1.24
$DOS(E_F)$	eV $f.u.^{-1}$	6.5

Table 4. Orbital filling and partial density of states at the Fermi level (in eV^{-1} per atom units) of $CeIr_3$.

	$CeIr_3$ GGA + SOC					$CeIr_3$ GGA+SOC+U				
	Ce(6c)	Ce(3a)	Ir(18h)	Ir(6c)	Ir(3b)	Ce(6c)	Ce(3a)	Ir(18h)	Ir(6c)	Ir(3b)
	(per atom)					(per atom)				
valence Q	4	4	9	9	9	4	4	9	9	9
Q (e)	2.69	2.50	7.52	7.52	7.48	2.08	1.85	7.67	7.67	7.69
Q *s*-states	0.18	0.15	0.55	0.55	0.54	0.19	0.15	0.55	0.52	0.54
Q p-states	0.33	0.31	0.42	0.42	0.39	0.33	0.31	0.43	0.39	0.40
Q *d*-states	1.11	0.98	6.48	6.48	6.48	1.32	1.16	6.62	6.68	6.69
Q *f*-states	1.04	1.05				0.21	0.20			
DOS(E_F)	1.21	2.22	0.72	0.72	0.61	0.22	0.28	0.59	0.74	0.52

Table 5. Orbital filling and partial density of states at the Fermi level (in eV^{-1} per atom units) of $LaIr_3$.

	$LaIr_3$ GGA+SOC				
	La(6c)	La(3a)	Ir(18h)	Ir(6c)	Ir(3b)
	(per atom)				
valence Q	3	3	9	9	9
Q (e)	1.17	1.05	7.51	7.46	7.50
Q *s*-states	0.08	0.07	0.55	0.52	0.55
Q p-states	0.32	0.31	0.40	0.37	0.37
Q *d*-states	0.61	0.53	6.49	6.51	6.51
Q *f*-states	0.15	0.14			
$DOS(E_F)$	0.16	0.20	0.94	1.29	1.27

Table 6. Density of states at the Fermi level, Sommerfeld coefficient and electron-phonon coupling constant calculated from heat capacity data as $\lambda_{e\text{-}p} = \gamma_{expt}/\gamma_{calc} - 1$, and by using the experimental Tc and inverted McMillan formula (with $\mu^* = 0.13$).

	$CeIr_3$ GGA+SOC	$CeIr_3$ GGA+SOC+U	$LaIr_3$ GGA+SOC
$DOS(E_F)$	4.31	2.42	3.9
γ_{calc}	10.16	5.71	9.2
γ_{expt}	25.1		11.5
$\lambda_{e\text{-}p} = \gamma_{expt}/\gamma_{calc} - 1$	1.47	3.4	0.25
$\lambda\ (T_c)$	0.63		0.55

References

1. Steglich, F. *et al.* Superconductivity in the Presence of Strong Pauli Paramagnetism: $CeCu_2Si_2$. *Phys. Rev. Lett.* **43,** 1892–1896 (1979).
2. Weng, Z. F., Smidman, M., Jiao, L., Lu, X. & Yuan, H. Q. Multiple quantum phase transitions and superconductivity in Ce-based heavy fermions. *Rep. Prog. Phys.* **79,** 094503 (2016).
3. Sologub, O., Salamakha, P., Gonçalves, A. P., Ipser, H. & Almeida, M. Crystal structure of the $CeIr_3$ compound. *J. Alloys Compd.* **373,** L5–L7 (2004).
4. Blazina, Z., Mohanty, R. C. & Raman, A. *Intermediate phases in some rare-earth-metal-iridium systems*. (Southern Univ., Baton Rouge, LA (USA), 1989).
5. Geballe, T. H. *et al.* Superconductivity in Binary Alloy Systems of the Rare Earths and of Thorium with Pt-Group Metals. *Phys. Rev.* **137,** A119–A127 (1965).
6. Sato, Y. J. *et al.* Superconducting Properties of $CeIr_3$ Single Crystal. *J. Phys. Soc. Jpn.* **87,** 053704 (2018).
7. Sheldrick, G. M & A. X. S. Bruker. *Inc., Madison, WI,* (2000)
8. Sheldrick, G. M. *XPREP*. (2001).
9. Sheldrick, G. M. A short history of SHELX. *Acta Crystallogr. Sect. A* **64,** 112–122 (2008).
10. Krill, G., Kappler, J. P., Meyer, A., Abadli, L. & Ravet, M. F. Surface and bulk properties of cerium atoms in several cerium intermetallic compounds: XPS and X-ray absorption measurements. *J. Phys. F Met. Phys.* **11,** 1713 (1981).
11. Blaha, P., Schwarz, K., Madsen G. K. H., Kvasnicka D. & Luitz J. *WIEN2K, An Augmented Plane Wave + Local Orbitals Program for Calculating Crystal Properties*. (2001).
12. Anisimov, V. I., Aryasetiawan, F. & Lichtenstein, A. I. First-principles calculations of the electronic structure and spectra of strongly correlated systems: the LDA + U method. *J. Phys. Condens. Matter* **9,** 767 (1997).

13. Anisimov, V. I. & Gunnarsson, O. Density-functional calculation of effective Coulomb interactions in metals. *Phys. Rev. B* **43,** 7570–7574 (1991).

14. Dong, R., Wan, X., Dai, X. & Savrasov, S. Y. Orbital-dependent electronic masses in Ce heavy-fermion materials studied via Gutzwiller density-functional theory. *Phys. Rev. B* **89,** 165122 (2014).

15. Novák, P., Kuneš, J., Chaput, L. & Pickett, W. E. Exact exchange for correlated electrons. *Phys. Status Solidi B* **243,** 563–572

16. Hakimi, M. & Huber, J. G. The valence of Ce in $CeRu_2$ and $CeIr_3$ thru superconductivity. *Phys. BC* **135,** 434–437 (1985).

17. Frank, F. C. & Kasper, J. S. Complex alloy structures regarded as sphere packings. I. Definitions and basic principles. *Acta Crystallogr.* **11,** 184–190 (1958).

18. Haldolaarachchige, N. *et al.* Ir d-band derived superconductivity in the lanthanum-iridium system $LaIr_3$. *J. Phys. Condens. Matter* **29,** 475602 (2017).

19. Górnicka, K. in preparation.

20. Kaczorowski, D. & Ślebarski, A. Kondo lattice behavior and magnetic ordering in $CeRh_2Si$. *Phys. Rev. B* **81,** 214411 (2010).

21. Kaczorowski, D. *et al.* Magnetic properties and electronic structures of intermediate valence systems $CeRhSi_2$ and $Ce_2Rh_3Si_5$. *J. Phys. Condens. Matter* **22,** 215601 (2010).

22. Pikul, A. P. *et al.* Giant crystal-electric-field effect and complex magnetic behavior in single-crystalline $CeRh_3Si_2$. *Phys. Rev. B* **81,** 174408 (2010).

23. Krawczyk, M., Holdynski, M., Lisowski, W., Sobczak, J. W. & Jablonski, A. Electron inelastic mean free paths in cerium dioxide. *Appl. Surf. Sci.* **341,** 196–202 (2015).

24. Qiu, L., Liu, F., Zhao, L., Ma, Y. & Yao, J. Comparative XPS study of surface reduction for nanocrystalline and microcrystalline ceria powder. *Appl. Surf. Sci.* **252,** 4931–4935 (2006).

25. Chowdhury, S. & Lin, K.-S. Characterization and surface reactivity analyses of ceria nanorod catalyst for methanol interaction. *Mater. Chem. Phys.* **133,** 163–169 (2012).

26. Paparazzo, E., Ingo, G. M. & Zacchetti, N. X-ray induced reduction effects at CeO_2 surfaces: An x-ray photoelectron spectroscopy study. *J. Vac. Sci. Technol. A* **9,** 1416–1420 (1991).

27. Ohno, Y. Core-electron spectra and electronic structure of $CeNbS_3$. *Phys. Rev. B* **48,** 5515–5524 (1993).

28. Fuggle, J. C. *et al.* Electronic structure of Ce and its intermetallic compounds. *Phys. Rev. B* **27,** 7330–7341 (1983).

29. Gunnarsson, O. & Schönhammer, K. Electron spectroscopies for Ce compounds in the impurity model. *Phys. Rev. B* **28,** 4315–4341 (1983).

30. Sales, B. C. & Wohlleben, D. K. Susceptibility of Interconfiguration-Fluctuation Compounds. *Phys. Rev. Lett.* **35,** 1240–1244 (1975).

31. Huber, J. G. Probing d-band superconductivity in XIr_3 compounds. *Phys. B Condens. Matter* **163,** 219–223 (1990).

32. Klimczuk, T. & Cava, R. J. Carbon isotope effect in superconducting $MgCNi_3$. *Phys. Rev. B* **70,** 212514 (2004).

33. Srivichitranond, L. C. *et al.* Superconductivity in a new intermetallic structure type based on endohedral $Ta@Ir_7Ge_4$ clusters. *Phys. Rev. B* **95,** 174521 (2017).

34. Strychalska-Nowak, J. *et al.* Fermi-liquid behavior of binary intermetallic compounds Y_3M (M = Co, Ni, Rh, Pd, Ir, Pt). *Mater. Res. Express* **4,** 066501 (2017).

35. Wiesmann, H. *et al.* Simple Model for Characterizing the Electrical Resistivity in A15 Superconductors. *Phys. Rev. Lett.* **38,** 782–785 (1977).

36. Hussey ǁ, N. E., Takenaka, K. & Takagi, H. Universality of the Mott–Ioffe–Regel limit in metals. *Philos. Mag.* **84,** 2847–2864 (2004).

37. Calandra, M. & Gunnarsson, O. Electrical resistivity at large temperatures: Saturation and lack thereof. *Phys. Rev. B* **66,** 205105 (2002).

38. Haldolaarachchige, N., Gibson, Q., Schoop, L. M., Luo, H. & Cava, R. J. Characterization of the heavy metal pyrochlore lattice superconductor $CaIr_2$. *J. Phys. Condens. Matter* **27,** 185701 (2015).

39. Barker, J. A. T. *et al.* Unconventional Superconductivity in La_7Ir_3 Revealed by Muon Spin Relaxation: Introducing a New Family of Noncentrosymmetric Superconductor That Breaks Time-Reversal Symmetry. *Phys. Rev. Lett.* **115,** 267001 (2015).

40. Mott, N. F. The electrical resistivity of liquid transition metals. *Philos. Mag. J. Theor. Exp. Appl. Phys.* **26,** 1249–1261 (1972).

41. Mott, N. F. Electrons in transition metals. *Adv. Phys.* **13,** 325–422 (1964).

42. Nagel, S. R. Thermoelectric Power and Resistivity in a Metallic Glass. *Phys. Rev. Lett.* **41,** 990–993 (1978).

43. McMillan, W. L. Transition Temperature of Strong-Coupled Superconductors. *Phys. Rev.* **167,** 331–344 (1968).

44. Verchenko, V. Y., Tsirlin, A. A., Zubtsovskiy, A. O. & Shevelkov, A. V. Strong electron-phonon coupling in the intermetallic superconductor Mo_8Ga_{41}. *Phys. Rev. B* **93,** 064501 (2016).

45. Singh, D., Hillier, A. D., Thamizhavel, A. & Singh, R. P. Superconducting properties of the noncentrosymmetric superconductor Re_6Hf. *Phys. Rev. B* **94,** 054515 (2016).

46. Carnicom, E. M. *et al.* $TaRh_2B_2$ and $NbRh_2B_2$: Superconductors with a chiral noncentrosymmetric crystal structure. *Sci. Adv.* **4,** eaar7969 (2018).

47. Werthamer, N. R., Helfand, E. & Hohenberg, P. C. Temperature and Purity Dependence of the Superconducting Critical Field, H_{c2}. III. Electron Spin and Spin-Orbit Effects. *Phys. Rev.* **147,** 295–302 (1966).

48. Helfand, E. & Werthamer, N. R. Temperature and Purity Dependence of the Superconducting Critical Field, H_{c2}. II. *Phys. Rev.* **147,** 288–294 (1966).
49. Chandrasekhar, B. S. BS Chandrasekhar, Appl. Phys. Lett. 1, 7 (1962). *Appl Phys Lett* **1,** 7 (1962).
50. Clogston, A. M. Upper Limit for the Critical Field in Hard Superconductors. *Phys. Rev. Lett.* **9,** 266–267 (1962).
51. Tinkham, M. *Introduction to Superconductivity*. (Courier Corporation, 1996).
52. Gschneidner, K. A., Eyring, L. & Hufner, S. Handbook on the physics and chemistry of rare earths, volume 10. (1987).
53. Kokalj A., Computer graphics and graphical user interfaces as tools in simulations of matter at the atomic scale, *Comp. Mater. Sci.* **28**, 155 (2003).Code available from http://www.xcrysden.org/